Active Power Factor Correction Converter Model for Harmonic Analysis in Common Mode and Differential Mode

Amin Gholizad, Jan Desmet, Jos Knockaert

***Abstract*—This study aims to investigate the frequency spectral characteristics of a simplified active power factor correction (APFC) converter. The proposed model is developed to predict harmonics present in both common mode (CM) and differential mode (DM) of the APFC converter up to 150 kHz. The proposed model is verified through simulation in MATLAB/Simulink. Both simulation and model are validated by experiments. The findings in this study can contribute significantly to understand the behavior of both harmonics and supraharmonics in APFC systems and aid in designing effective filters for mitigating their negative effects on both low frequency and high frequency power quality.**

***Index Terms*—Active Power Factor Correction Converters, AC to DC converters, common mode, differential mode, supraharmonics**

I. Introduction

APFC converters have gained significant popularity in recent years for powering single-phase loads. The main driver are the IEC standards [1] aiming at limiting harmonic current emissions of electronic devices. These converters are employed as part of the power conditioning system and typically placed behind the diode bridge rectifier (DBR) in AC-DC power supplies. Controllable semiconductor switch based DC-DC converters, such as boost, buck and, fly-back converters at the DBR output are a common type of APFC converters used to improve the power factor and reduce harmonic content [2]–[5]. To meet specific power factor standards, these converters are controlled to emulate a resistive input behavior in grid frequency, which is essential for improving the power factor and reducing the total harmonic distortion (THD) in the system [5], [6].

Simplified equivalent circuits are used to examine system harmonics. These circuits are employed to streamline the study of harmonic components within a system, facilitating a more efficient and generalized examination of the system frequency response in similar and higher frequency studies [7]–[10]. In [7] a detailed boost converter model is developed for CM and DM study in $[150\,kHz - 1\,MHz]$ frequency range. This method works by modeling the switch as a high frequency voltage source using the waveform of the voltage across the switch in a switching period. Then an equivalent circuit for CM and DM respectively is created in order to calculate the respective currents. Authors of [8] modeled boost converter in DC systems for EMI analysis using CM and DM equivalent circuits for filter design purposes.

Understanding supraharmonics CM and DM behaviors in power converters is essential for improving their EMI performance and ensuring reliable operation. Previous research has primarily focused on to model and analyze DM noise [9]–[13], CM noise has not received the same level of attention in the supraharmonics range $[2\,kHz - 150\,kHz]$. In [9], [10], the same modeling approach as [7] is used with considerations for the supraharmonics such as idealized square pulse, therefore ignoring rise and fall times, and approximating input impedance to the boost inductor, however only DM noise is studied. Fourier series is a powerful tool in the frequency domain analysis and is mainly used for modeling various converter topologies. In [11] a single phase boost converter is modeled for DM filter calculations for frequency range larger than $150\,kHz$. The Fourier series is used to calculate the switch node voltage and the current is then calculated by dividing it with the boost inductive reactance. In [12] Totem pole converters are modeled in supraharmonics for DM noise estimation using Fourier series. A CM and DM model using Fourier series for three-phase rectifiers is presented in [14] for frequencies up to $3\,kHz$.

This paper proposes a simpler yet effective novel model using Fourier series for simultaneously analyzing both CM and DM noise in APFC converters up to $150\,kHz$. Similar models for studying high frequency distortions of the three phase motor drives [15] and bridge rectifiers [16] are proved to be representative and useful in filter design. This model can produce accurate approximations around 80% faster compared to simulation software. This is particularly useful in multi-device studies, such as interleaved converters, for reducing CM and DM noise [17]–[19], where several converters are utilized with a phase shifted carrier for switching in order to increase power output and decrease filter size by shifting the noise to higher frequencies.

The rest of the paper is elaborated as follows. In section II the proposed model is explained. Firstly, the expressions for the different states of the converter is derived using circuit analysis . Then these expressions are used to derive positive side current $i_p(t)$ and negative side current $i_n(t)$, and then they are used to calculate CM and DM currents as seen by the grid. In section III the model is validated through simulation and experiment. The analytical results with simulation using MATLAB/Simulink and experimental data obtained from the lab setup is compared. Finally, in section IV the paper is concluded. The results show proposed model is comparable to detailed simulations, and experiments for both CM and DM

currents considering the speed improvements of the proposed model.

II. APFC Converter Model

A. Conventional APFC Converters

The fly-back, push-pull converters are popular in APFC applications as they provide galvanic isolation and can be used to either output lower or higher voltages than the input voltage typically by changing the transformer ratio. Boost converter is the simplest converter that is usually used in literature for modeling. This model works can be used for boost converter as well. The circuit diagram of these converters are shown in Fig. 1. In order to simplify the model, the converter impedance can be approximated by an RL load for frequencies less than $150\,kHz$. Fig. 2 gives the MATLAB simulation results comparing the comprehensive models impedance and approximated impedance up to $150\,kHz$. It is evident that the impedance of the comprehensive model exhibits characteristics similar to an RL load within this frequency range.

B. Proposed Simplified Model

In simplifying an AC-DC converter to its essential components, the following elements can be considered (Fig. 3):

1. DBR: It is comprised of four diodes. The primary objective of the DBR is to convert AC from the grid into DC. The diodes are considered as ideal switches.
2. Load: The load refers to any device or appliance that consumes power from the DC bus. This could be anything from motors, LED lighting, batteries for renewable energy storage systems, or other electronic circuits. However, since the grid side behavior of the APFC is inductive-resistive, regardless of the load, in the proposed simple model a resistor is used to model this load. The inductive part of the model is assigned to the filter inductor. This model is also simulated in MATLAB and compared to the comprehensive model, as shown in Fig. 2. As can be observed, it exhibits even better approximation than RL load. The filter inductor is in series with the grid impedance, and for simplicity they are not considered in developing this model. However, it can be added back in for calculating its effect on interferences.
3. Switching semiconductor (MOSFETs, IGBTs): The switching semiconductor controls the power flow by switching between open and closed state at high switching frequency. Instantaneous switching will be assumed for simplification purposes as suggested in [9].
4. Capacitive coupling: A capacitor is utilized to address the parasitic capacitive coupling between the switch, load and ground. This parasitic capacitor is connected to the drain of the MOSFET/IGBT since this pin is usually connected to the backplate of its package where a heatsink is attached to. The backplate and heatsink are electrically isolated by the thermal compound. The heatsink is connected to the ground. This type of connection creates the aforementioned parasitic capacitor [20]. This capacitor is the main source of CM noise and

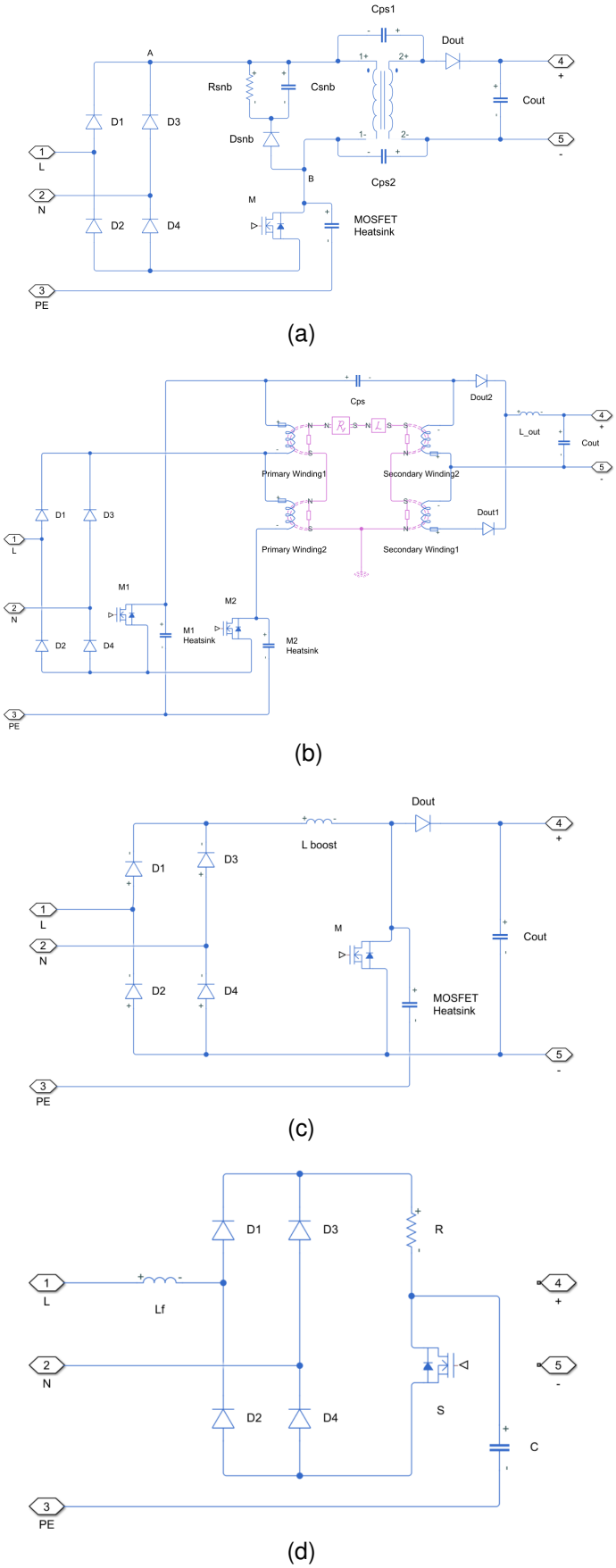

Fig. 1. Typical converter schematics (a) fly-back (b) push-pull (c) boost (d) proposed model.

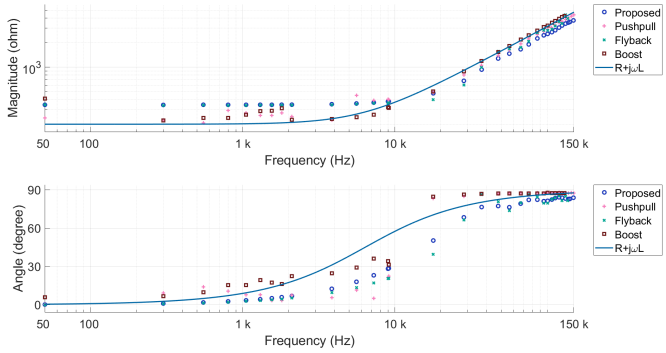

Fig. 2. Impedance comparison of several detailed APFC models and proposed approximation.

secondary side parasitic capacitances can be neglected [21].

The proposed simplified APFC converter for developing the model is shown in Fig. 3.

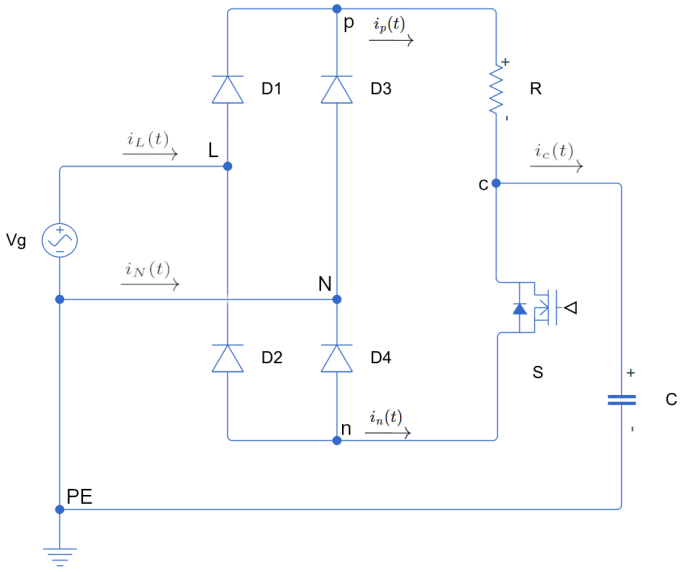

Fig. 3. Simplified circuit of APFC converter, including parasitic capacitor for CM path.

C. Grid Voltage

For modeling the grid source, the flat top voltage waveform exemplify the typical voltages found in residential, commercial and industrial networks, as elaborated in [22]. When constructing a model for a single load in a power system, it is common to assume zero impedance for input voltage source at the load's terminals. In this scenario, the interactions with the power supply system, including impedance effects, can be incorporated within a broader simulation framework such as iterative harmonic analysis (IHA) for conducting system-level studies [13].

The grid voltage is expressed by (1), where $V_{g,max}[V]$ denotes the nominal amplitude of the grid voltage, $r_{ft}[unitless]$ represents the ratio between the flat-top and nominal amplitude, and $\omega_g\left[\frac{rad}{s}\right]$ is the grid angular frequency.

$$v_g(t) = \begin{cases} r_{ft}V_{g,max} & V_{g,max}\sin(\omega_g t) \geq r_{ft}V_{g,max} \\ -r_{ft}V_{g,max} & V_{g,max}\sin(\omega_g t) \leq -r_{ft}V_{g,max} \\ V_{g,max}\sin(\omega_g t) & o.w \end{cases} \tag{1}$$

The grid voltage is depicted in Fig. 4, exhibiting all harmonics and higher odd harmonics as evident in Fig. 4b. Therefore, we can also represent the grid voltage as its Fourier series equivalent:

$$v_g(t) = \sum_{n=-\infty}^{\infty} \mathbf{c}_{v_g}[n]\mathbf{e}^{\mathbf{j}n\omega_g t} \tag{2}$$

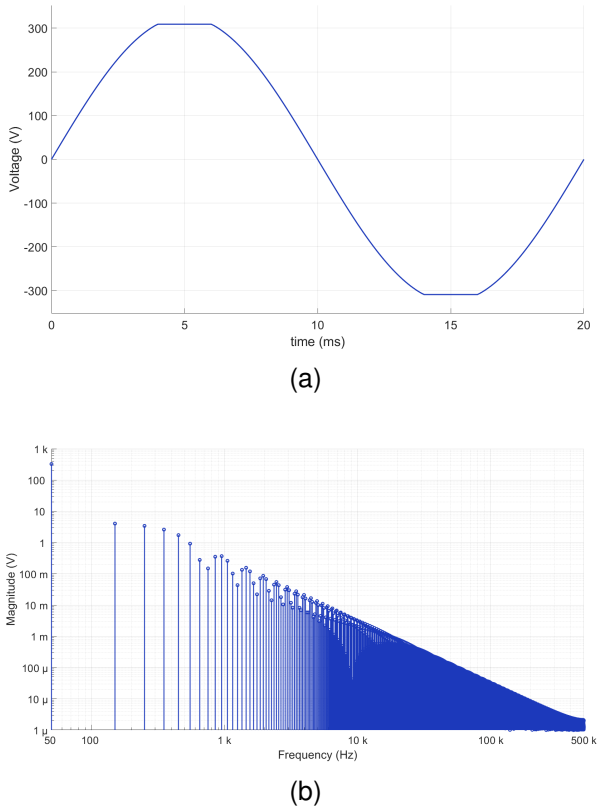

Fig. 4. Flat top grid voltage with $r_{ft} = 95\%$ (a) time domain (b) frequency spectrum.

D. Currents In Each State

The simplified circuit has four states, which depend on the sign of the grid voltage $\mathrm{sgn}(V_g(t))$ and the state of the switch $s(t)$,(Fig. 5).

1) State A: As depicted in Fig. 5a, the grid voltage is positive, the switch is off. $D1$ is in forward bias while $D2$ and $D3$ are in reverse bias. $D4$ is not connected. Consequently, the circuit simplifies to a RC circuit. In this state, the currents are defined as follows: $i_{L,A}(t) = i_{p,A}(t) = i_{c,A}(t)$, $i_{N,A}(t) = 0$, and $i_{n,A}(t) = 0$. For the RC circuit we can write:

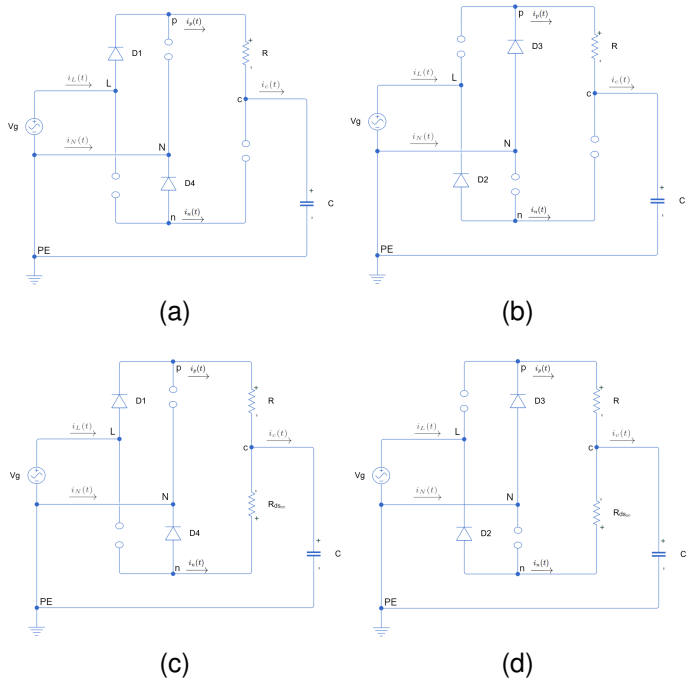

Fig. 5. Different states of the simplified circuit (a) $\text{sgn}(V_g(t)) = 1$, $s(t) = 0$, (b) $\text{sgn}(V_g(t)) = -1$, $s(t) = 0$, (c) $\text{sgn}(V_g(t)) = 1$, $s(t) = 1$, (d) $\text{sgn}(V_g(t)) = -1$, $s(t) = 1$.

$$\begin{aligned} v_g(t) &= v_R(t) + v_C(t) \\ &= i_{p,A}(t)R + v_c(t_0) + \frac{1}{C}\int_{t_0}^{t} i_{p,A}(t)dt \\ \xrightarrow{\frac{d}{dt}} \frac{dv_g(t)}{dt} &= R\frac{di_{p,A}(t)}{dt} + \frac{1}{C}i_{p,A}(t) \end{aligned} \tag{3}$$

By solving (3) for $i_{p,A}(t)$ the coefficients can be derived as follows:

$$\begin{aligned} i_{p,A}(t) &= A_A\mathbf{e}^{-\frac{1}{RC}t} + \sum_{n=-\infty}^{\infty}\mathbf{c}_{i_{p,A}}[n]\mathbf{e}^{\mathbf{j}n\omega_g t} \\ &where: \\ \mathbf{c}_{i_{p,A}}[n] &= \frac{Cn\omega_g\mathbf{c}_{v_g}[n]}{CRn\omega_g - \mathbf{j}} \end{aligned} \tag{4}$$

2) State B: As shown in Fig. 5b, the grid voltage is negative, and the switch is off. $D1$ and $D4$ are in reverse bias, while $D3$ is in forward bias, and $D2$ is not connected. In this state, the circuit reduces to R connected to C, and the grid voltage is disconnected from the load. Therefore, the currents are defined as follows: $i_{N,B}(t) = i_{p,B}(t) = i_{c,B}(t)$, $i_{L,B}(t) = 0$, and $i_{n,B}(t) = 0$. Since state B happens following state D and in this state D3 is in forward bias, assuming its larger reverse recovery time compared to the discharge time of the capacitor, the capacitor discharges through R. Therefore the current is:

$$i_{p,B}(t) = i_{c,B}(t) = A_B\mathbf{e}^{-\frac{t}{RC}} \tag{5}$$

3) State C: In Fig. 5c, the grid voltage is positive, and the switch is on. Both $D1$ and $D4$ are in forward bias, while $D2$ and $D3$ are in reverse bias. The load (R) is in series with the parallel combination of $R_{ds_{on}}$ and C in this state. The currents are related by $i_{L,C}(t) = i_{p,C}(t)$, and $i_{N,C}(t) = i_{n,C}(t)$. In this case (Fig. 5c) capacitor voltage can be calculated as:

$$\begin{aligned} i_{c,C}(t) =& i_{p,C}(t) + i_{n,C}(t) \\ C\frac{dv_{c,C}(t)}{dt} =& \frac{v_g(t) - v_{c,C}(t)}{R} - \frac{v_{c,C}(t)}{R_{ds_{on}}} \\ v_{c,C}(t) =& A_C\mathbf{e}^{-\frac{R+R_{ds_{on}}}{RCR_{ds_{on}}}t} + \sum_{n=-\infty}^{\infty}\mathbf{c}_{v_c,C}[n]\mathbf{e}^{\mathbf{j}n\omega_g t} \\ \mathbf{c}_{v_c,C}[n] =& \frac{R_{ds_{on}}\mathbf{c}_{v_g}[n]}{R + R_{ds_{on}} + \mathbf{j}CRR_{ds_{on}}n\omega_g} \end{aligned} \tag{6}$$

therefore, using (6) $i_{c,C}(t)$, $i_{p,C}(t)$ and $i_{n,C}(t)$ coefficients are as follows:

$$\begin{aligned} i_{c,C}(t) =& C\frac{dv_{c,C}(t)}{dt} \\ =& A_{c,C}\mathbf{e}^{-\frac{R+R_{ds_{on}}}{RCR_{ds_{on}}}t} + \sum_{n=-\infty}^{\infty}\mathbf{c}_{i_{c,C}}[n]\mathbf{e}^{\mathbf{j}n\omega_g t} \\ \mathbf{c}_{i_{c,C}}[n] =& \frac{CR_{ds_{on}}n\omega_g\mathbf{c}_{v_g}[n]}{CRR_{ds_{on}}n\omega_g - \mathbf{j}(R + R_{ds_{on}})} \\ A_{c,C} =& -\frac{R + R_{ds_{on}}}{RR_{ds_{on}}}A_C \end{aligned} \tag{7}$$

$$\begin{aligned} i_{p,C}(t) =& \frac{v_g(t) - v_{c,C}(t)}{R} \\ =& A_{p,C}\mathbf{e}^{-\frac{R+R_{ds_{on}}}{RCR_{ds_{on}}}t} + \sum_{n=-\infty}^{\infty}\mathbf{c}_{i_{p,C}}[n]\mathbf{e}^{\mathbf{j}n\omega_g t} \\ \mathbf{c}_{i_{p,C}}[n] =& \frac{CR_{ds_{on}}n\omega_g\mathbf{c}_{v_g}[n] - \mathbf{j}\mathbf{c}_{v_g}[n]}{CRR_{ds_{on}}n\omega_g - \mathbf{j}(R + R_{ds_{on}})} \\ A_{p,C} =& -\frac{A_C}{R} \end{aligned} \tag{8}$$

$$\begin{aligned} i_{n,C}(t) =& -\frac{v_c(t)}{R_{ds_{on}}} \\ =& A_{n,C}\mathbf{e}^{-\frac{R+R_{ds_{on}}}{RCR_{ds_{on}}}t} + \sum_{n=-\infty}^{\infty}\mathbf{c}_{i_{n,C}}[n]\mathbf{e}^{\mathbf{j}n\omega_g t} \\ \mathbf{c}_{i_{n,C}}[n] =& -\frac{\mathbf{c}_{v_g}[n]}{R + R_{ds_{on}} + \mathbf{j}CRR_{ds_{on}}n\omega_g} \\ A_{n,C} =& -\frac{A_C}{R_{ds_{on}}} \end{aligned} \tag{9}$$

4) State D: In Fig. 5d, the grid voltage is negative, and the switch is on. $D1$ and $D4$ are in reverse bias, while $D2$ and $D3$ are in forward bias. In this state, $R_{ds_{on}}$ is in series with the parallel combination of R and C. The currents are related by $i_{L,D}(t) = i_{n,D}(t)$, and $i_{N,D}(t) = i_{p,D}(t)$. This case is similar to state C, with the distinction in the connections of L and N to n and p, respectively. The capacitor voltage in this case is:

$$
\begin{aligned}
i_{c,D}(t) =& i_{p,D}(t) + i_{n,D}(t) \\
C\frac{dv_{c,D}(t)}{dt} =& \frac{v_g(t) - v_{c,D}(t)}{R_{ds_{on}}} - \frac{v_{c,D}(t)}{R} \\
v_{c,D}(t) =& A_D \mathbf{e}^{-\frac{R+R_{ds_{on}}}{RCR_{ds_{on}}}t} + \sum_{n=-\infty}^{\infty} \mathbf{c}_{v_c,D}[n]\mathbf{e}^{\mathbf{j}n\omega_g t} \\
\mathbf{c}_{v_c,D}[n] =& \frac{R\mathbf{c}_{v_g}[n]}{R + R_{ds_{on}} + \mathbf{j}CRR_{ds_{on}}n\omega_g}
\end{aligned} \tag{10}
$$

therefore using (10) $i_{c,D}(t)$, $i_{p,D}(t)$ and $i_{n,D}(t)$ coefficients will be calculated as:

$$
\begin{aligned}
i_{c,D}(t) =& C\frac{dv_{c,D}(t)}{dt} \\
=& A_{c,D}\mathbf{e}^{-\frac{R+R_{ds_{on}}}{RCR_{ds_{on}}}t} + \sum_{n=-\infty}^{\infty} \mathbf{c}_{i_{c,D}}[n]\mathbf{e}^{\mathbf{j}n\omega_g t} \\
\mathbf{c}_{i_{c,D}}[n] =& \frac{CRn\omega_g \mathbf{c}_{v_g}[n]}{CRR_{ds_{on}}n\omega_g - \mathbf{j}(R + R_{ds_{on}})} \\
A_{c,D} =& -\frac{R + R_{ds_{on}}}{RR_{ds_{on}}}A_D
\end{aligned} \tag{11}
$$

$$
\begin{aligned}
i_{p,D}(t) =& \frac{-v_{c,D}(t)}{R} \\
=& A_{p,D}\mathbf{e}^{-\frac{R+R_{ds_{on}}}{RCR_{ds_{on}}}t} + \sum_{n=-\infty}^{\infty} \mathbf{c}_{i_{p,D}}[n]\mathbf{e}^{\mathbf{j}n\omega_g t} \\
\mathbf{c}_{i_{p,D}}[n] =& -\frac{\mathbf{c}_{v_g}[n]}{R + R_{ds_{on}} + \mathbf{j}CRR_{ds_{on}}n\omega_g} \\
A_{p,D} =& -\frac{A_D}{R}
\end{aligned} \tag{12}
$$

$$
\begin{aligned}
i_{n,D}(t) =& \frac{v_g(t) - v_c(t)}{R_{ds_{on}}} \\
=& A_{n,D}\mathbf{e}^{-\frac{R+R_{ds_{on}}}{RCR_{ds_{on}}}t} + \sum_{n=-\infty}^{\infty} \mathbf{c}_{i_{n,D}}[n]\mathbf{e}^{\mathbf{j}n\omega_g t} \\
\mathbf{c}_{i_{n,D}}[n] =& \frac{CRn\omega_g \mathbf{c}_{v_g}[n] - \mathbf{j}\mathbf{c}_{v_g}[n]}{CRR_{ds_{on}}n\omega_g - \mathbf{j}(R + R_{ds_{on}})} \\
A_{n,D} =& -\frac{A_D}{R_{ds_{on}}}
\end{aligned} \tag{13}
$$

E. Transients

As can be seen from (4), (5), (7) to (9) and (11) to (13) the currents have a transient part that can be generalized as the following:

$$
tr_y(t) = A_{y,x}\mathbf{e}^{-t/\tau_y} \tag{14}
$$

In turn-off the capacitor will be charged up to $|v_g(t)|$ with a time constant of $\tau_{off} = RC$ and in turn-on the capacitor will be discharged to a small value according to $\frac{R_{ds_{on}}}{R+R_{ds_{on}}}|v_g(t)|$ with time constant of $\tau_{on} = \frac{RCR_{ds_{on}}}{R+R_{ds_{on}}}$. Therefore in a switching period the on-transients:

$$
\begin{aligned}
tr_{on,x}(t) =& \begin{cases} -A_{on,x}\mathbf{e}^{-\frac{t}{\tau_{on}}} & 0 \le t < DT_{sw} \\ 0 & DT_{sw} \le t < T_{sw} \end{cases} \\
\mathbf{c}_{tr_{on,x}}[n] =& -\frac{A_{on,x}\tau_{on}\left(1 - \mathbf{e}^{-\frac{T_{sw}D}{\tau_{on}} - \mathbf{j}2n\pi D}\right)}{T_{sw} + \mathbf{j}2n\pi\tau_{on}}
\end{aligned} \tag{15}
$$

and off-transients will be:

$$
\begin{aligned}
tr_{off,x}(t) =& \begin{cases} 0 & 0 \le t < DT_{sw} \\ A_{off,x}\mathbf{e}^{-\frac{t-DT_{sw}}{\tau_{off}}} & DT_{sw} \le t < T_{sw} \end{cases} \\
\mathbf{c}_{tr_{off,x}}[n] =& \frac{\mathbf{j}A_{off,x}\tau_{\text{off}}\left(\mathbf{e}^{-\mathbf{j}2n\pi D} - \mathbf{e}^{\frac{T_{sw}(D-1)}{\tau_{\text{off}}}}\right)}{-2n\pi\tau_{\text{off}} + \mathbf{j}T_{sw}}
\end{aligned} \tag{16}
$$

However, as mentioned $A_{y,x}$ depends on the value of the grid voltage at the switching moment. If we assume the grid period is much larger than the switching period ($T_g \gg T_{sw}$), we can assume $v_g(t)$ remains constant during a switching period. The area under the current curve for consecutive $tr_{off,x}$ and $\frac{R+R_{ds_{on}}}{RR_{ds_{on}}}tr_{on,x}$ should be the same. Therefore we can find the ratio between $\frac{A_{on,x}}{A_{off,x}}$ as:

$$
\frac{A_{on}}{A_{off}} = \frac{\int_{DT_{sw}}^{T_{sw}} \mathbf{e}^{-\frac{t-DT_{sw}}{\tau_{off}}}\,dt}{\frac{R+R_{ds_{on}}}{RR_{ds_{on}}}\int_0^{DT_{sw}} \mathbf{e}^{-\frac{t}{\tau_{on}}}\,dt} \tag{17}
$$

To factor the grid voltage dependency in $A_{y,x}$ within a grid cycle we can multiply a normalized factor of grid voltage to these transients:

$$
\begin{aligned}
tr_{off}(t) &= \frac{v_g(t)}{r_{ft}V_{g,max}}tr_{off,x} \\
tr_{on}(t) &= \frac{v_g(t)}{r_{ft}V_{g,max}}tr_{on,x}
\end{aligned} \tag{18}
$$

1) Repeating Square Pulse: A repeating square pulse can be described as:

$$
x_T(t) = \begin{cases} 1 & |t| \le \frac{T_p}{2} \\ 0 & |t| > \frac{T_p}{2} \end{cases} \qquad -\frac{T}{2} < t \le \frac{T}{2} \tag{19}
$$

where T_p is the on-time. This waveform has the following Fourier series:

$$
\begin{aligned}
x_T(t) =& \sum_{n=-\infty}^{\infty} \mathbf{c}_{X_T}[n]\mathbf{e}^{\mathbf{j}n\omega_T t} \\
&\text{where:} \\
\mathbf{c}_{X_T}[n] =& D\,\mathrm{sinc}(n\pi D) \\
\mathrm{sinc}(x) =& \frac{\sin x}{x}
\end{aligned} \tag{20}
$$

where $D = \frac{T_p}{T}$ is the duty cycle. However, in order to start the pulse at $t = 0$ we have a shift of $\frac{T_p}{2}$. In Fourier series this translates to multiplying $\mathbf{c}_{X_T}[n]$ with $\mathbf{e}^{-\mathbf{j}n\pi D}$. Therefore, we can define the switching function $s(t)$ as follows:

$$s(t) = \begin{cases} 1 & 0 \le t \le T_p \\ 0 & T_p < t \le T_{sw} \end{cases} \qquad 0 < t \le T_{sw}$$
$$= \sum_{n=-\infty}^{\infty} \mathbf{c}_s[n] \mathbf{e}^{\mathbf{j}n\omega_{sw}t} \tag{21}$$
where:
$$\mathbf{c}_s[n] = D\mathbf{e}^{-\mathbf{j}n\pi D}\,\mathrm{sinc}(n\pi D)$$

and similarly we can define AC voltage polarity $p(t)$ using a pulse with $D = 50\%$ as:

$$p(t) = \begin{cases} 1 & V_g(t) \ge 0 \\ 0 & V_g(t) < 0 \end{cases} \qquad 0 < t \le T_g$$
$$= \sum_{n=-\infty}^{\infty} \mathbf{c}_p[n] \mathbf{e}^{\mathbf{j}n\omega_g t} \tag{22}$$
where:
$$\mathbf{c}_p[n] = \frac{1}{2}\mathbf{e}^{-\mathbf{j}\frac{n\pi}{2}}\,\mathrm{sinc}(\frac{n\pi}{2})$$

Let us also define:

$$\bar{s}(t) = 1 - s(t)$$
$$\mathbf{c}_{\bar{s}}[n] = \begin{cases} 1 - D & n = 0 \\ -D\mathbf{e}^{-\mathbf{j}\frac{n\pi}{2}}\,\mathrm{sinc}(n\pi D) & o.w \end{cases} \tag{23}$$

$$\bar{p}(t) = 1 - p(t)$$
$$\mathbf{c}_{\bar{p}}[n] = \begin{cases} \frac{1}{2} & n = 0 \\ -\frac{1}{2}\mathbf{e}^{-\mathbf{j}\frac{n\pi}{2}}\mathrm{sinc}\left(\frac{n\pi}{2}\right) & o.w \end{cases} \tag{24}$$

2) Other Representation Of The Currents: Using the definitions in previous sections the currents can be rewritten as:

$$\begin{aligned} i_c(t) =& (i_{c,A}(t) \cdot p(t) + i_{c,B}(t) \cdot \bar{p}(t)) \cdot \bar{s}(t) \\ &+ (i_{c,C}(t) \cdot p(t) + i_{c,D}(t) \cdot \bar{p}(t)) \cdot s(t) \\ i_p(t) =& (i_{p,A}(t) \cdot p(t) + i_{p,B}(t) \cdot \bar{p}(t)) \cdot \bar{s}(t) \\ &+ (i_{p,C}(t) \cdot p(t) + i_{p,D}(t) \cdot \bar{p}(t)) \cdot s(t) \\ i_n(t) =& (i_{n,C}(t) \cdot p(t) + i_{n,D}(t) \cdot \bar{p}(t)) \cdot s(t) \end{aligned} \tag{25}$$

F. Common Mode And Differential Mode Currents

In order to get phase and neutral currents using $i_p(t)$ and $i_n(t)$ we can use the fact that:

$$\begin{aligned} i_L(t) &= \begin{cases} i_p(t), & v_g(t) \ge 0 \\ i_n(t), & v_g(t) < 0 \end{cases} \\ i_N(t) &= \begin{cases} i_n(t), & v_g(t) \ge 0 \\ i_p(t), & v_g(t) < 0 \end{cases} \end{aligned} \tag{26}$$

The CM and DM currents can be defined by:

$$\begin{aligned} i_{CM}(t) =& \frac{i_L(t) + i_N(t)}{2} = \begin{cases} \frac{i_p(t)+i_n(t)}{2}, & v_g(t) \ge 0 \\ \frac{i_n(t)+i_p(t)}{2}, & v_g(t) < 0 \end{cases} \\ =& \frac{i_p(t) + i_n(t)}{2} = \frac{i_c(t)}{2} \end{aligned} \tag{27}$$

$$\begin{aligned} i_{DM}(t) =& \frac{i_L(t) - i_N(t)}{2} = \begin{cases} \frac{i_p(t)-i_n(t)}{2}, & v_g(t) \ge 0 \\ \frac{i_n(t)-i_p(t)}{2}, & v_g(t) < 0 \end{cases} \\ =& \frac{i_p(t) - i_n(t)}{2} \cdot sgn_{v_g}(t) \end{aligned}$$

Since $i_{DM}(t)$ depends on the sign of the $v_g(t)$ we need to define it. As we know, the harmonics of the grid voltage are small compared to the fundamental harmonic ($V_n \ll V_1, \quad n \ge 2$) meaning positive and negative half cycles of the fundamental can determine the positivity and negativity of the total grid voltage.

$$\begin{aligned} sgn_{v_g}(t) =& \mathrm{sgn}\left(v_g(t)\right) = \mathrm{sgn}\left(\sum_{n=1}^{\infty} V_n \sin(n\omega_g t)\right) \\ \xrightarrow[n\ge 2]{V_n \ll V_1} & = \mathrm{sgn}(\sin(\omega_g t)) = \sum_{n=-\infty}^{\infty} \mathbf{c}_{sgnv}[n] \mathbf{e}^{\mathbf{j}n\omega_g t} \end{aligned} \tag{28}$$
where:
$$\mathbf{c}_{sgnv}[n] = \begin{cases} -\frac{2i}{n\pi} & n = 2k+1,\ k \in \mathbb{Z} \\ 0 & o.w \end{cases}$$

Therefore, we can write

$$i_{CM}(t) = \sum_{n=-\infty}^{\infty} \mathbf{c}_{CM}[n] \mathbf{e}^{\mathbf{j}n\omega_g t}$$
where:
$$\begin{aligned} \mathbf{c}_{CM}[n] =& \frac{1}{2}(\mathbf{c}_{i_{c,A}}[n] * \mathbf{c}_p[n] + \mathbf{c}_{tr_{off}}[n]) * \mathbf{c}_{\bar{s}}[n] \\ &+ \frac{1}{2}\left(\mathbf{c}_{i_{c,C}}[n] * \mathbf{c}_p[n] + \mathbf{c}_{i_{c,D}}[n] * \mathbf{c}_{\bar{p}}[n] + \frac{R + R_{ds_{on}}}{RR_{ds_{on}}}\mathbf{c}_{tr_{on}}[n]\right) \\ &* \mathbf{c}_s[n] \end{aligned} \tag{29}$$

and for $i_{DM}(t)$:

$$i_{DM}(t) = \sum_{n=-\infty}^{\infty} \mathbf{c}_{DM}[n] \mathbf{e}^{\mathbf{j}n\omega_g t}$$
where:
$$\begin{aligned} \mathbf{c}_{DM}[n] =& \frac{1}{2}\left(\mathbf{c}_{i_{p,A}}[n] * \mathbf{c}_p[n] + \mathbf{c}_{tr_{off}}[n] * \mathbf{c}_{sgnv}[n]\right) * \mathbf{c}_{\bar{s}}[n] \\ &+ \frac{1}{2}\left(\left(\mathbf{c}_{i_{p,C}}[n] - \mathbf{c}_{i_{n,C}}[n]\right) * \mathbf{c}_p[n]\right) * \mathbf{c}_s[n] \\ &- \frac{1}{2}\left(\left(\mathbf{c}_{i_{p,D}}[n] - \mathbf{c}_{i_{n,D}}[n]\right) * \mathbf{c}_{\bar{p}}[n]\right) * \mathbf{c}_s[n] \\ &+ \frac{R_{ds_{on}} - R}{2RR_{ds_{on}}}\mathbf{c}_{tr_{on}}[n] * \mathbf{c}_{sgnv}[n] * \mathbf{c}_s[n] \end{aligned} \tag{30}$$

Note that $(*)$ is the convolution in (29) and (30).

III. Simulation And Experimental Results

In this section, the simplified model is validated utilizing analytical, simulation, and experimental techniques.

A. Analytical Approximation

The multiplication of two functions in time domain, become a convolution in the frequency domain:

$$\begin{aligned} f(t) &= \sum_{n=-\infty}^{\infty} F[n]\mathbf{e}^{\mathbf{j}n\frac{2\pi}{T}t} \\ g(t) &= \sum_{n=\infty}^{\infty} G[n]\mathbf{e}^{\mathbf{j}n\frac{2\pi}{T}t} \\ h(t) &= f(t)\cdot g(t) \\ &= \sum_{n=\infty}^{\infty} H[n]\mathbf{e}^{\mathbf{j}n\frac{2\pi}{T}t} \end{aligned} \tag{31}$$

where

$$H[n] = F[n] * G[n] = \sum_{m=-\infty}^{\infty} F[m]\cdot G[n-m]$$

However, computing this infinite sum is not feasible and to have a good accuracy we will use ± 10000 iterations which covers up to $500\,kHz$ for $50\,Hz$ harmonics. Therefore:

$$H[n] = F[n] * G[n] \approx \sum_{m=-10000}^{10000} F[m]\cdot G[n-m] \tag{32}$$

MATLAB scripts are utilized for analytical calculations. The relevant parameters are gathered in Table. I.

TABLE I
Setup parameters

parameter	value
$V_{g,max}$	$230\sqrt{2}\,V$
r_{ft}	95%
F_g	$50\,Hz$
F_{sw}	$20\,kHz$
R	$200\,\Omega$
$R_{ds_{on}}$	$0.5\,\Omega$
D	50%
C	$4.80\,nF$

The duty cycle of the APFC converters depends on the loading at the DC side however as the load approaches full load it becomes relatively constant compared to a lower loading as can be seen from simulation results in two different loading conditions in Fig. 6. Considering a full load, the duty cycle of the model is considered a constant value. For reliability reasons the maximum allowed duty cycle is usually set to 50%. Which we have chosen for the our study cases.

Since the model is defined in frequency domain any non-linear frequency dependent impedance of the grid including the inductive part of the model can be used in conjunction for more realistic grid impedance calculations when using iterative methods. For the study cases grid impedance is set as

$$R_{dc} + k\sqrt{\omega} + \mathbf{j}L\omega \tag{33}$$

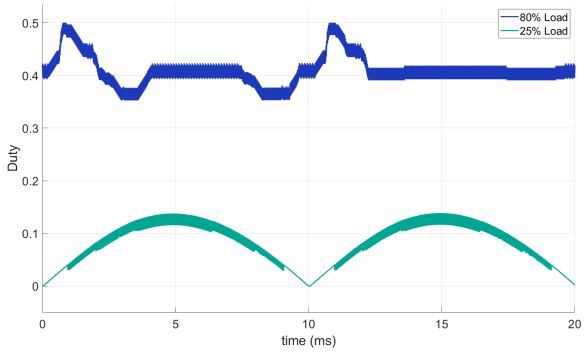

Fig. 6. Simulation results for duty cycle variation over a $50\,Hz$ cycle for different loading conditions.

in order to consider skin effect in the transmission lines where $R_{dc} = 100\,m\Omega$, $k = 0.01$ and $L = 100\,\mu H$.

B. Simulation Model

The MATLAB/Simulink Simscape electrical toolbox is employed for simulation. The diodes and the switch are represented by linear models. The diodes have a $0.6\,V$ forward voltage, $0.3\,\Omega$ on-state resistance, and $100\,M\Omega$ off-state resistance. The switch has a $0.5\,\Omega$ on-state resistance and $100\,M\Omega$ off-state resistance. The simulation time is set to $20\,ms$, since the simplified model does not require additional time to reach steady state in contrast to a full detailed model. This makes the simplified model much faster to simulate compared to the detailed model. The step size of $1\,\mu s$ is chosen since it is an integer multiple of both grid and switching frequencies. Also the corresponding sampling frequency ($1\,MHz$) is high enough to properly capture frequency responses in the supraharmonics range. These conditions are necessary in order to compute FFT correctly. For demonstration purposes, capacitance effect is also run for $F_{sw} = 20005Hz$ which requires $200\,ms$ and $0.49988\,\mu s$ for proper FFT.

C. Experimental Setup

In the experimental setup, two LPSA800H1000JB $100\,\Omega$ $800\,W$ resistors are connected in series as load. The diode bridge is the BU2006-E3/45 and the switch is the SIHP24N80AEF-GE3 N-Channel MOSFET. All the heatsinks of the resistors and the MOSFET are linked to the PE port of the power outlet. For current measurement, three Tektronix TCP312A probes with TCPA300 amplifiers are utilized and a PicoScope 5444D is utilized both for capturing signals and for generating pulses to control the switch.

D. Comparison And Results

As it can be seen from Fig. 8a the prediction of the harmonics levels is within $\pm 5\,dB$ in CM and less than $\pm 0.5\,dB$ in DM for the analytical results compared to the experimental results at the switching frequency. The larger difference in CM noise is due to it being more sensitive to grid conditions. The analytical results are within $\pm 0.2\,dB$ and

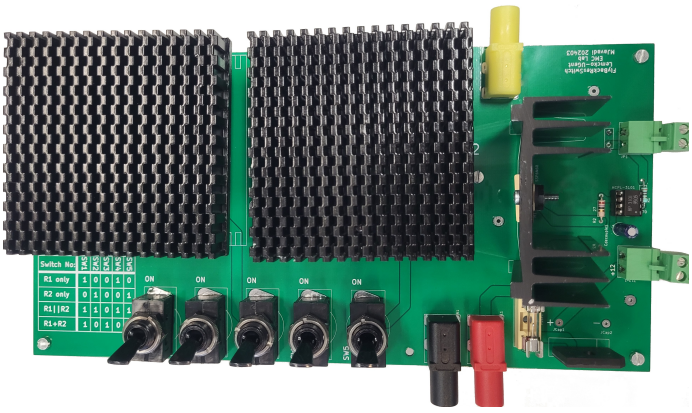

Fig. 7. Experimental setup.

$\pm 0.02dB$ compared to simulations at the switching frequency in CM and DM current respectively, suggesting their accuracy is almost identical.

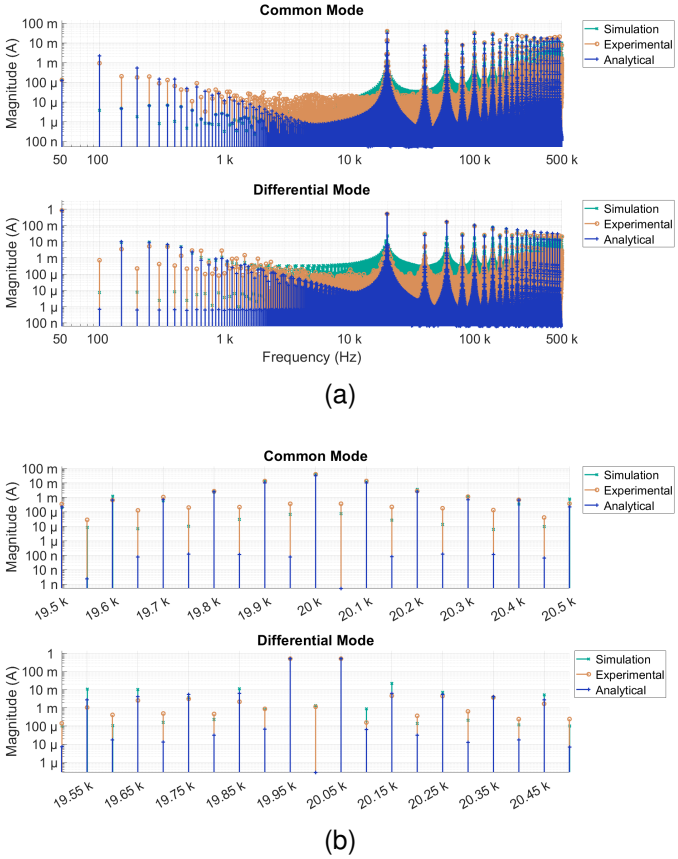

Fig. 8. Comparison of analytical approximation, simulation and experimental CM and DM currents (a) full spectrum (b) around switching frequency.

From Fig. 8b we can see that in CM the switching frequency F_{sw} and the sidebands $F_{sw} \pm 2kF_g$ are dominant harmonics. In DM the sidebands $F_{sw} \pm (2k+1)F_g$ are dominant. This means in CM the even multiples of the grid frequency occur as sidebands and in DM odd multiples of grid frequency.

E. Impedance Impact On Interferences

The inductance of iron core transformers and inductors depends on the frequency as follows [23]:

$$Z = ((R_w + R_c + \mathbf{j}\omega L)^{-1} + \mathbf{j}\omega C_{res})^{-1} \tag{34}$$

where R_w is winding loses R_c is core losses and C_{res} is stray capacitance of the inductor. In frequencies less than $150\,kHz$ the total series resistance $R_s = R_w + R_c$ can be simplified as $R_s = r\omega$ where r is a constant value. considering $r = 1 \times 10^{-5}\Omega/Hz$, $L = 95\,\mu H$ $C_{res} = 56.6\,pF$ as measured in [23], the current harmonics are compared to no impedance case, a linear inductance of the same value and the grid impedance from (33) as shown in Fig. 9. The nonlinear inductance decreases the harmonic at $20\,kHz$ by $1.5\,dB$ in CM and 0.05dB in DM at $20.05\,kHz$.

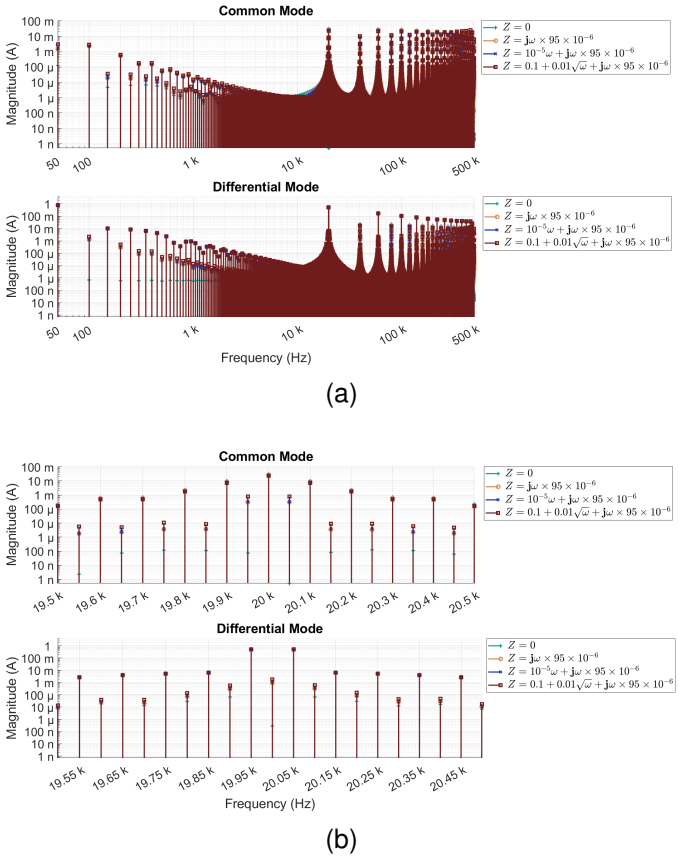

Fig. 9. Impedance effect on current harmonics for different scenarios (a) full spectrum (b) at switching frequency neighborhood.

F. Model Speed Comparison

For speed assessment of the proposed method, two cases are considered as fallowing:

1) Sensitivity Analysis: By using the provided model it is possible to check for the impact of each parameter on the emissions. For illustration purposes, the parasitic capacitor value is changed from $1\,pF$ to $1\,\mu F$ with 100 points per decade and shown in Fig. 10. As it can be seen from Fig. 10a as the capacitance increases the switching harmonics as well as grid

harmonics increase. However, the change in capacitance has negligible effect on the DM as shown in Fig. 10b.

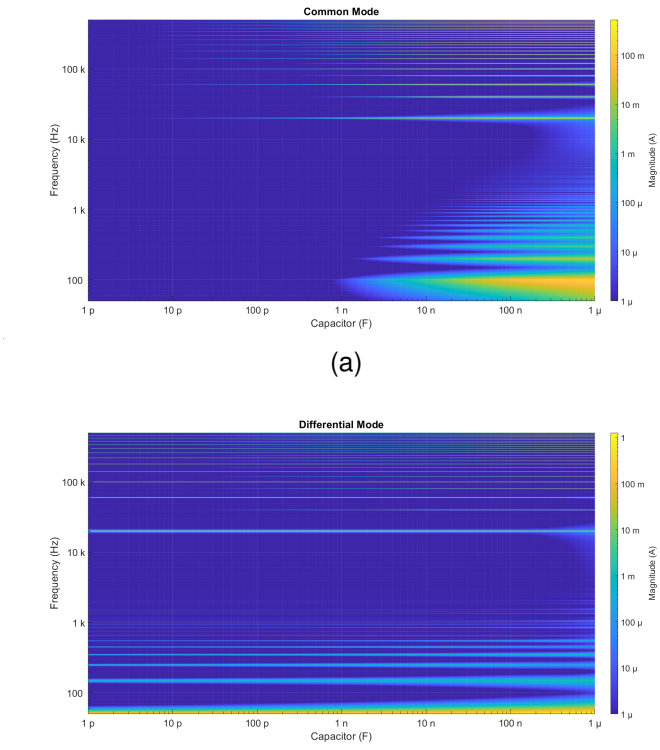

Fig. 10. Parasitic capacitance effect on (a) CM (b) DM.

For validating these findings the parasitic capacitance of the experimental model is also changed by adding several capacitors in parallel to the MOSFET heatsink. the measurement results are shown in Fig. 11. As can be seen from Fig. 11, the CM harmonics increase with increasing capacitance and DM harmonics are not effected.

2) Interleaved APFC: Another interesting application of this model is in studying aggregate behavior of several switching loads in the system. For demonstration purposes, 60 similar loads are used in parallel and effect of phase deference between the switching frequency of them in the total current is shown in Fig. 12. The first converter is set as the reference (i.e., $\phi_0 = 0$) and the phase of the other converters is defined as:

$$\phi_i = i \times \Delta\Phi \qquad i = 0, 1, 2, \ldots, 59 \tag{35}$$

where $\Delta\Phi$ is the phase shift value in the horizontal axis in Fig. 12. As can be seen, low frequency harmonics are not effected by this change, however, switching frequency and its harmonics are showing have a different behavior in different phase shifts for example all switching harmonics are zero when $\Delta\Phi = k \times \frac{360^\circ}{60^\circ} = k \times 6^\circ, k \in \mathrm{Z}$. However the sidebands in the first harmonic increase as $\Delta\Phi$ approaches 0° and decreases as $\Delta\Phi$ approaches 180°. The second harmonic increases around 0° and 180° and decreases around 90° and 270°. The third harmonic is lower at even $\Delta\Phi$ except at multiples of 120° at which it is even higher than odd $\Delta\Phi$

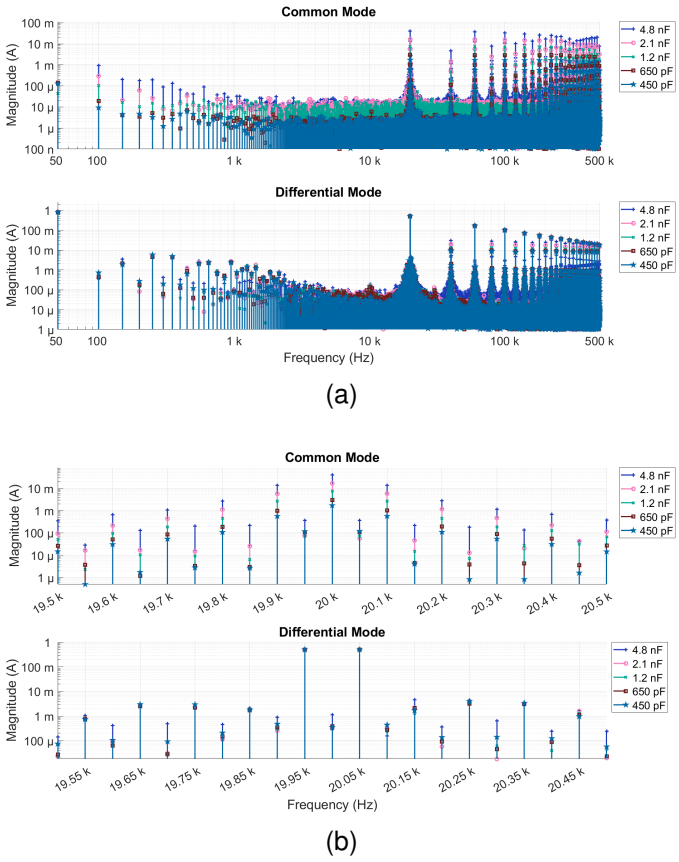

Fig. 11. Experimental results for different capacitance of the parasitic capacitance (a) full spectrum (b) around switching frequency.

and has more sidebands. Other harmonics have also similar patterns. Therefore, it can be concluded that even though the $\kappa\frac{360^\circ}{n}$ phase shift for interleaving is a good way of mitigating the switching harmonics it is not the only solution and in case of imperfect synchronization other possible phase shifts can have lower emissions in lower harmonic orders.

For speed comparison, the same graph is generated using the MATLAB/Simulink software leveraging parallel simulations on a 8-core i7-11800H laptop with 16Gb ram and the time is measured for both analytical calculations and simulations several times and the average results are summarized in Fig. 13. As it can be seen there is a 75% and 86% speed improvement compared to simulation for Fig. 10 and Fig. 12, respectively. And in the case of $F_{sw} = 20005\,Hz$ the proposed method is still 40% faster.

IV. Conclusion

This paper provides a simplified model of an APFC converter. The goal is to investigate the behavior of CM and DM currents preserving low frequency and high frequency details in the converter in a fast and efficient way. It demonstrates that this model can be used to analyze larger systems that include APFC converters and predict the system behavior much faster than using conventional simulation software without losing much accuracy for both in low and high frequency power quality analysis.

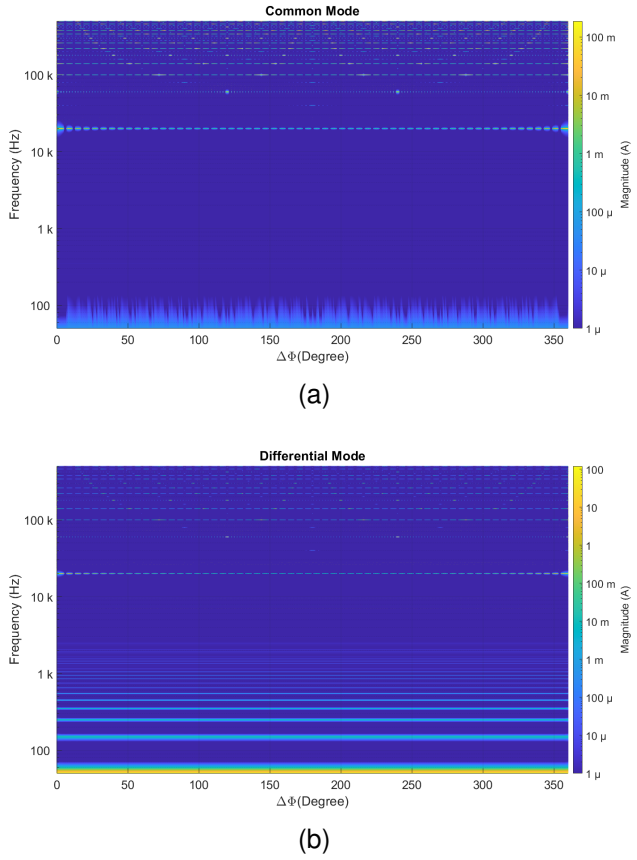

Fig. 12. Phase deference effect on (a) CM (b) DM for $\mathbf{c}_p = 250\,pF$.

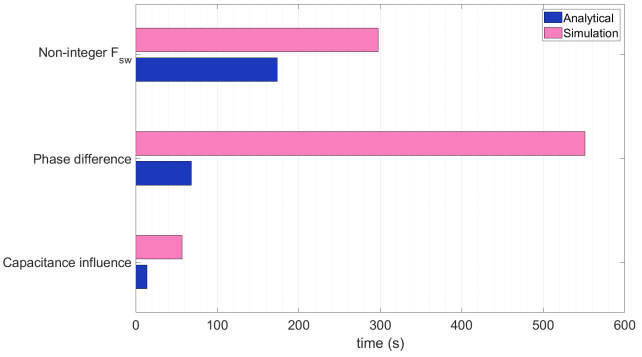

Fig. 13. Time comparison for calculating Fig. 10 and Fig. 12 with the proposed method and simulation.

The analytical results are validated through simulation using MATLAB/Simulink and experimental data obtained from the lab setup. The results show proposed model is comparable to detailed simulations, and experiments for both CM and DM currents while being 80% faster than simulations.

V. Acknowledgement

This research is funded by Flanders Innovation & Entrepreneurship and is part of the cSBO project IMPERFECT (HBC.2021.0175).

References

[1] *Limits for harmonic current emissions (equipment input less than 16 A per phase), IEC 61000-3-2*. 2018.

[2] Z. Chen, J. Qi, X. Chen, and J. Xu, "Hybrid Converter Cell-Based Buck-Type Bridgeless PFC Converters With Low THD," in *2023 IEEE 6th International Electrical and Energy Conference (CIEEC)*, 2023, pp. 2221–2226.

[3] X. Liu, Y. Wan, M. He, Q. Zhou, and X. Meng, "Buck-Type Single-Switch Integrated PFC Converter With Low Total Harmonic Distortion," *IEEE Transactions on Industrial Electronics*, vol. 68, no. 8, pp. 6859–6870, Aug. 2021.

[4] M. Prajapati and Nair. R. Viju, "Design Considerations in the Control of Single Phase Boost Power Factor Corrected Rectifier for Utility Applications," in *2021 International Conference on Sustainable Energy and Future Electric Transportation (SEFET)*, 2021, pp. 1–6.

[5] K. De Gusseme, W. R. Ryckaert, D. M. Van de Sype, J. A. Ghijselen, J. A. Melkebeek, and L. Vandevelde, "A Boost PFC Converter With Programmable Harmonic Resistance," *IEEE Transactions on Industry Applications*, vol. 43, no. 3, pp. 742–750, May 2007.

[6] C. Lee Sirio, "Analysis of Line Current Harmonics for Single-Phase PFC Converters," in *2007 IEEE Power Electronics Specialists Conference*, 2007, pp. 1291–1297.

[7] Q. Ji, X. Ruan, L. Xie, and Z. Ye, "Conducted EMI Spectra of Average-Current-Controlled Boost PFC Converters Operating in Both CCM and DCM," *IEEE Transactions on Industrial Electronics*, vol. 62, no. 4, pp. 2184–2194, Apr. 2015.

[8] C. Wanklad and P. Pairodamonchai, "Common-mode and Differential-mode Equivalent Circuits for EMI Analysis in Boost Converter," in *2023 20th International Conference on Electrical Engineering/Electronics, Computer, Telecommunications and Information Technology (ECTI-CON)*, 2023, pp. 1–4.

[9] N. Nourani Esfetanaj, H. Wang, F. Blaabjerg, and P. Davari, "Differential Mode Noise Prediction and Analysis in Single-Phase Boost PFC for the New Frequency Range of 9–150 kHz," *IEEE Journal of Emerging and Selected Topics in Industrial Electronics*, vol. 3, no. 1, pp. 177–187, Jan. 2022.

[10] N. N. Esfetanaj, S. Peyghami, H. Wang, and P. Davari, "Analytical Modeling of 9-150 kHz EMI in Single-Phase PFC Converter," in *IECON 2019 - 45th Annual Conference of the IEEE Industrial Electronics Society*, 2019, vol. 1, pp. 4689–4693.

[11] Rahamadullah, N. Beedu, and R. Ranjan, "Differential Mode filter design with Analytical model of Single Phase PFC Boost Converter for Avionics Applications," in *2023 11th National Power Electronics Conference (NPEC)*, 2023, pp. 1–5.

[12] A. Tausif and S. Dusmez, "A Unified Differential Mode Noise Estimation Method and Filter Size Comparison in Single-Phase Multileg and Multilevel Totem-Pole PFC Converters," *IEEE Transactions on Power Electronics*, vol. 38, no. 6, pp. 7197–7206, Jun. 2023.

[13] A. J. Collin, J. Drapela, R. Langella, and A. Testa, "Emission assessment of single-phase switch-mode PFC loads up to 150 kHz: Experimental analysis and modelling," *Electric Power Systems Research*, vol. 220, p. 109236, Jul. 2023.

[14] Z. Zhang, A. Zingariello, and G. Griepentrog, "A Frequency-domain Model of Common-Mode and Differential-Mode Sources in Three Phase Diode Rectifier Systems," in *2023 IEEE Symposium on Electromagnetic Compatibility & Signal/Power Integrity (EMC+SIPI)*, 2023, pp. 643–648.

[15] W. Shen, F. Wang, and D. Boroyevich, "Conducted EMI characteristic and its implications to filter design in 3-phase diode front-end converters," in *Conference Record of the 2004 IEEE Industry Applications Conference, 2004. 39th IAS Annual Meeting.*, 2004, vol. 3, pp. 1840–1846 vol.3.

[16] S. Qu and D. Chen, "Mixed-mode EMI noise and its implications to filter design in offline switching power supplies," *IEEE Transactions on Power Electronics*, vol. 17, no. 4, pp. 502–507, Jul. 2002.

[17] M. A. Rahman, Y. Sozer, and J. A. De Abreu-Garcia, "Reduction of Electromagnetic Interference (EMI) in Interleaved DC-DC Converters," in *2020 IEEE Energy Conversion Congress and Exposition (ECCE)*, 2020, pp. 3552–3557.

[18] P. Koch, C. E. S. Feloups, N. Moonen, and F. Leferink, "Common-Mode EMI Reduction Control Strategy for Interleaved Converters," *IEEE Letters on Electromagnetic Compatibility Practice and Applications*, vol. 6, no. 2, pp. 79–83, Jun. 2024.

[19] Y. Yang, M. Mu, Z. Liu, F. C. Lee, and Q. Li, "Common mode EMI reduction technique for interleaved MHz critical mode PFC converter with coupled inductor," in *2015 IEEE Energy Conversion Congress and Exposition (ECCE)*, 2015, pp. 233–239.

[20] B. Zhang and X. Wang, "EMI and EMC of Switching Power Converters," in *Chaos Analysis and Chaotic EMI Suppression of DC-DC Converters*, IEEE, 2013, pp. 93–108.
[21] C. E. S. Feloups, H. H. Adhena, N. Moonen, D. Thomas, and F. Leferink, "Investigating the CM Noise Generated by Different Configurations of Multiple Forward Converters," in *2023 International Symposium on Electromagnetic Compatibility – EMC Europe*, 2023, pp. 1–6.
[22] *IEC, "Harmonics and interharmonics including mains signalling at a.c. Power port, low frequency immunity tests," IEC 61000-4-13 A1 Ed.1, Sec. 8.2.1*. 2015.
[23] T. Ewald and J. Biela, "Frequency-Dependent Inductance and Winding Loss Model for Gapped Foil Inductors," *IEEE Transactions on Power Electronics*, vol. 37, no. 10, pp. 12370–12379, Oct. 2022.

Amin Gholizad was born in Naghadeh, Iran, in July 1991. He received the B.Sc. degree in electrical engineering (power) and the M.Sc. degree in electrical engineering (power electronics) from the Department of Electrical Engineering, Urmia University, Urmia, Iran, in 2013 and 2016, respectively. He is currently pursuing the Ph.D. degree with the Department of Electromechanical, Systems and Metal Engineering, Ghent University, Kortrijk, Belgium.,His current research interests include power electronic converters, power quality, electromagnetic compatibility, renewable energy, and electrical vehicle chargers.

Jan J. M. Desmet (°1960) received the Polytechnical Engineer degree from the polytechnic academy in Kortrijk, the M.Sc. degree in Electrical Engineering from the V.U.Brussels and his PhD. degree at the K.U.Leuven, Belgium. Currently he is senior full professor at the Ghent University teaching Renewable Energy Sources and (μ)Grid integration. His research interests include PQ, LV distributed generation, renewables, storage and hosting capacity. Besides his job as senior full professor and researcher, he also is member of several expert groups and both reviewer and topic chairman for international scientific conferences. He is also IEEE senior member, member of SC77A (IEC) and TC210 (CENELEC). His international scientific recognition is validated by his membership of the CIRED Technical Committee TC2 and several PhD juries abroad. Besides that, he was also member of the EASAC - 'Dedicated Storage on Electrical Power Systems' advisory board for the EU commission. His research lab is the only one over Europe with a free programmable artificial grid of 240kVA, including all renewable sources and 2 45 kVA 4Q-controlled AC/DC sources. Since November 2014, research group EELab/Lemcko became member of the prestigious DERLab group. Jan Desmet is (co)author of more than 80 contributions published in international peer reviewed journals, 5 international technical reports and more than 100 conference papers. Finally he is also member of the academic board of the Belgium TNO and member of the strategic team for the Flemish DNO.

Jos Knockaert (M'09- SM'19) received the degree of industrial engineer in Electrotechnics in 1996 from the University College of Bruges-Ostend, the M.Sc. degree in Electronic System Design in 2001 from Leeds Metropolitan University and the Ph.D. degree in Engineering Science in 2009 from the K.U. Leuven. He worked as EMC-design engineer in the industry. He founded and is running the EMC laboratory in Ghent University since more than 10 years, supporting companies in finding solution for EMI problems. Currently, he is associate professor with Ghent University, teaching electrical machines, electromagnetic compatibility and power electronics. He is member of the research group Lemcko with focus on high frequency problems in low voltage grids and industrial systems.